Chemical Science

This article can be cited before page numbers have been issued, to do this please use: X. Zheng, X. Miao, Z. Yang, Z. Luo, J. Yu, H. Li and L. Zhang, *Chem. Sci.*, 2025, DOI: 10.1039/D5SC04431F.

ROYAL SOCIETY OF CHEMISTRY

rsc.li/chemical-science

View Article Online
DOI: 10.1039/D5SC04431F

ARTICLE

Structurally Engineered CNT-Confined $Mn_xRu_{1-x}O_2$ Catalysts for Efficient Acidic Oxygen Evolution at Low Ru Loading

Received 00th January 20xx,
Accepted 00th January 20xx

DOI: 10.1039/x0xx00000x

Xiaolin Zheng, [a†] Xiaofei Miao, [ab†] Zijie Yang [a], Zhaoyan Luo [a], Jun Yu [a], Huiqi Li, [*a] and Lei Zhang [*a]

Developing acidic oxygen evolution reaction (OER) catalysts with low noble metal loading and high activity remains a critical challenge for advancing proton exchange membrane water electrolyzers. Herein, we report a structurally engineered $Mn_xRu_{1-x}O_2$ catalysts confined on carbon nanotubes (CNTs), enabling highly dispersed active sites and remarkable catalytic activity at low Ru content. The uniform nanoscale coating of $Mn_xRu_{1-x}O_2$ along CNT sidewalls promotes Mn-O-Ru interfacial bonding and establishes an electron-bridge for enhances charge transfer. The optimized CNT-$(Mn_{0.75}Ru_{0.25})O_2$ catalyst delivers a -low overpotential of 120 mV at 10 mA cm^{-2} and an exceptional mass activity of 5549 A g_{Ru}^{-1} at 270 mV—252 times that of commercial RuO_2 (22 A g_{Ru}^{-1}). Combined X-ray spectroscopy, *in-situ* Raman, and differential electrochemical mass spectrometry reveal that the electron-rich Ru centers stabilized by Mn-O bridges accelerate charge transfer and suppress Ru dissolution during OER. Moreover, the CNT substrate and Ru incorporation synergistically generate abundant oxygen vacancies, significantly enhancing the catalytic activity through an improved lattice oxygen-mediated mechanism. This work highlights the critical role of CNT confinement and interfacial electronic modulation in decoupling noble metal usage from performance, offering a versatile design strategy for next-generation acidic OER catalysts

Introduction

Proton exchange membrane water electrolyzers (PEMWEs) offer a promising route for sustainable hydrogen production due to their high current densities, rapid system response, and superior energy efficiency.[1–3] However, the harsh oxidative and acidic environment on the anode side necessitates the use of noble metal-based oxygen evolution reaction (OER) catalysts, primarily Ru and Ir, which significantly increases system cost and limits large-scale deployment.[4–7]

Over the past decade, efforts to reduce noble metal usage in acidic OER catalysts have led to two competing trends: either maximizing intrinsic activity per noble metal atom (e.g., via single-atom or heteroatom doping strategies), or lowering overpotential at the cost of increased loading. Yet, these approaches often encounter an inherent trade-off between activity and noble metal content. Few systems can simultaneously deliver overpotentials below 150 mV at 10 mA cm^{-2} and mass activities above 3000 A g_{Ru}^{-1}, as required for practical application.[8–13] In addition, many Ru-based materials undergo irreversible structural degradation due to the lattice oxygen-mediated mechanism (LOM), wherein lattice oxygen directly participates in O-O bond formation, accelerating metal dissolution and catalyst collapse.[14–16]

To overcome these limitations, a triple strategy is essential: (i) enhancing the atomic utilization of Ru via uniform dispersion, (ii) modulating the electronic structure to suppress the dissolution of active site Ru atoms, and (iii) improving catalyst activity through the introduction of abundant oxygen vacancies.[17–20] Such an approach offers a promising pathway to break the traditional activity-cost-stability trade-off and enable the rational design of high performance and stable acid OER catalysts.

Herein, we report a structurally engineered $Mn_xRu_{1-x}O_2$ catalyst uniformly grown along carbon nanotube (CNT) sidewalls, forming a confined nanoscale interface that enables homogeneous Ru dispersion and C-Mn-O-Ru electronic coupling. Beyond physical confinement, CNTs play additional roles in modulating the catalyst structure and properties. During hydrothermal synthesis, CNTs react with $KMnO_4$ to form

---

[a] College of Chemistry and Environmental Engineering, Shenzhen University, Shenzhen, 518060, P.R. China
[b] College of Biomedical Engineering, Shenzhen University, Shenzhen, 518060, P.R. China

† These authors contributed equally to this work.

Correspondence and requests for materials should be addressed to H. L. (huiqili@szu.edu.cn) or L.Z. (lei.zhang@szu.edu.cn).

Supplementary Information available: [details of any supplementary information available should be included here]. See DOI: 10.1039/x0xx00000x

View Article Online
DOI: 10.1039/D5SC04431F

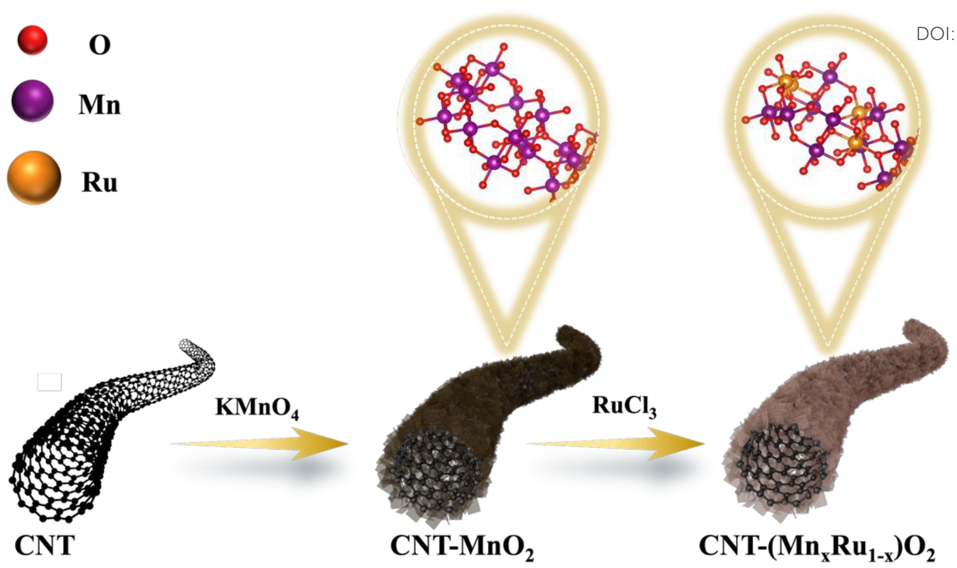

Scheme 1. Schematic illustration of the synthesis of CNT–$(Mn_{1-x}Ru_x)O_2$. $KMnO_4$ oxidizes CNT to form MnO_2-coated CNT (CNT-MnO_2), followed by $RuCl_3$ treatment to generate Ru-substituted $(Mn_{1-x}Ru_x)O_2$ domains confined on the CNT surface. The inset highlights the atomic- highlights the atomic-level incorporation of Ru into the MnO_2 lattice, forming CNT-Mn-O-Ru bridges.

chemically bonded MnO_2 coatings, introducing oxygen vacancies and promoting uniform oxide dispersion. In addition, the CNTs enhance electrical conductivity, facilitate directional electron transfer from CNT to Mn and then to Ru via Mn–O bridges, and mitigates structural degradation under acidic conditions.

These effects collectively contribute to the stabilization of Ru in a partially reduced state, suppressing over-oxidation and improving OER performance. As a result, the optimized CNT-confined $(Mn_{0.75}Ru_{0.25})O_2$ catalyst delivers a low overpotential of 120 mV at 10 mA cm^{-2} a mass activity of 5549 A g_{Ru}^{-1} at 270 mV, outperforming commercial RuO_2 and the majority of reported Ru-based acidic OER catalysts. Comprehensive spectroscopic and electrochemical analyses reveal that the synergy of CNT confinement and interfacial electronic modulation is key to achieving high activity, low Ru loading, and enhanced stability. This work provides a viable pathway toward the design of cost-effective, durable acidic OER catalysts for scalable hydrogen production.

Results and discussion

Materials synthesis and characterization

To illustrate the synthesis strategy and structural evolution of our catalyst, a schematic diagram is shown in Scheme 1. Pristine carbon nanotubes (CNTs) were oxidized using $KMnO_4$ to form a MnO_2 shell, followed by $RuCl_3$ treatment to introduce Ru and generate $(Mn_xRu_{1-x})O_2$ [x = 0.7-0.9, based on the inductively coupled plasma (ICP) result of Ru to Mn] alloy on the CNT surface (see Methods). To validate the proposed catalyst design, the crystalline structure of the catalysts was first analyzed using X-ray diffraction (XRD, Figure S1). All samples exhibit a characteristic peak near 12.5°, characteristic of the tetragonal α-MnO_2 phase (PDF#44-0141), distinguishing it from other MnO_2 phases.[21] Meanwhile, with no detectable peaks associated with RuO_2 and metallic Ru, indicating successful incorporation of Ru into the MnO_2 lattice. Transmission electron microscopy (TEM) and high-angle annular dark-field scanning transmission electron microscopy (HAADF-STEM) were then employed to investigate the morphology and dispersion. As shown in Figure 1a and Figure S2, the oxide forms a continuous coating across the CNT surface, exhibiting nanoscale roughness and island-like surface features, with no apparent nanoparticle aggregation. This nanoscale confinement is critical for stabilizing the active phase and preventing particle growth, as observed in the previous studies.[14,18,22] Elemental mapping (Figure 1b) reveals a homogeneous distribution of Mn, Ru, and O across CNT surfaces, which further indicates the formation of alloy rather than phase separation. High-resolution STEM images (Figure 1c-e) exhibit distinct lattice fringes with spacings of 0.27 nm and 0.31 nm, corresponding to the (400) and (310) planes of α-MnO_2, respectively. Moreover, intensity profiles (Figure 1f-h and Figure S3) show variations in atomic contrast consistent with Ru atoms substituting Mn within the oxide lattice. These structural features collectively indicate that Ru is incorporated into the MnO_2 lattice, forming a homogeneous $Mn_xRu_{1-x}O_2$ solid solution.

To further understand the electronic structure and coordination environment of CNT-$(Mn_xRu_{1-x})O_2$ catalysts, X-ray photoelectron spectroscopy (XPS) and X-ray absorption spectroscopy (XAS) analyses were conducted.[23–25] The Mn $2p_{3/2}$ peak of CNT-MnO_2 exhibits a 0.4 eV negative shift relative to that of MnO_2, indicating that the introduction of CNTs promotes electron transfer from CNT to Mn. For CNT-$(Mn_{0.75}Ru_{0.25})O_2$, the Mn $2p_{3/2}$ peak shows a 0.24 eV positive shift compared to CNT-MnO_2, suggesting that Ru doping increases the oxidation state of Mn, leading to electron loss by Mn (Figure 2a). When

View Article Online
DOI: 10.1039/D5SC04431F

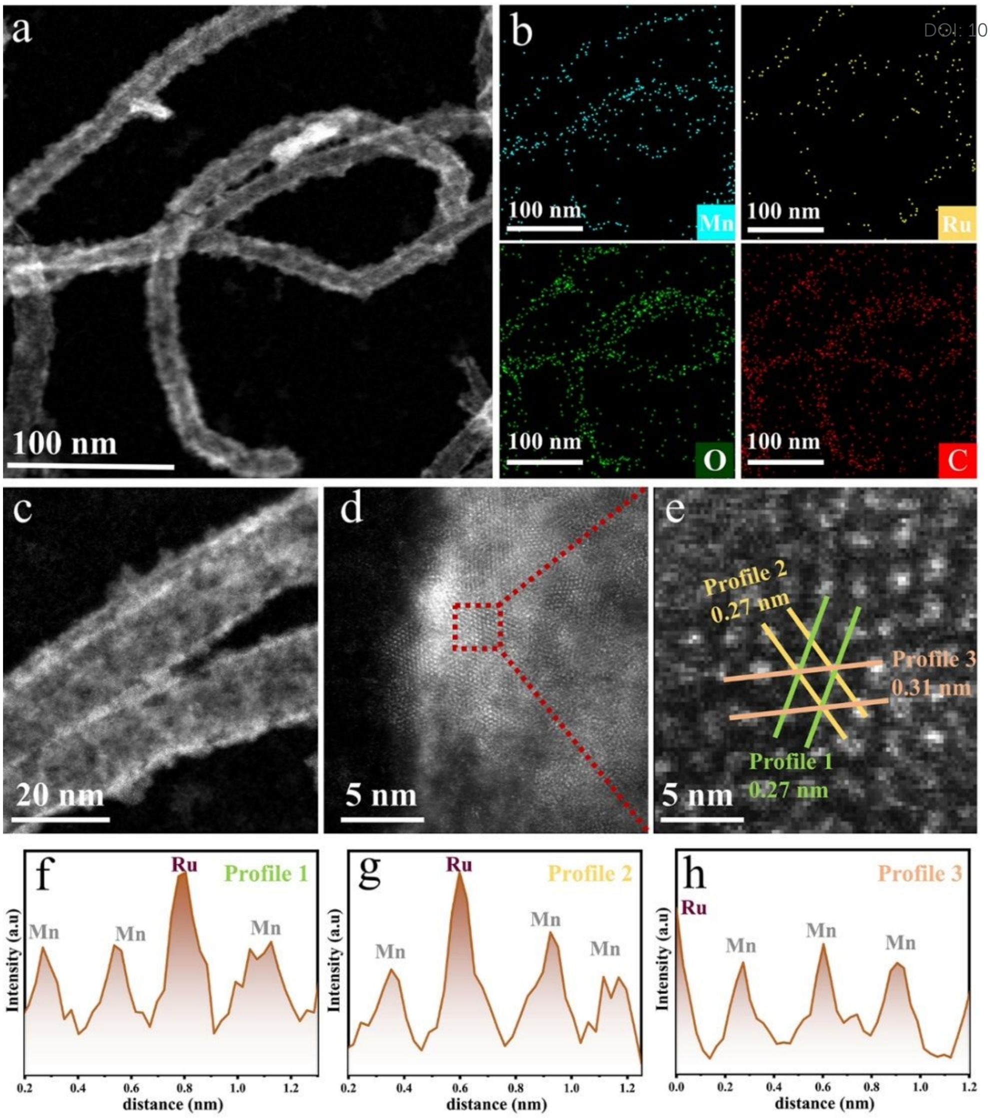

Figure 1. (a) HAADF-STEM image of CNT-($Mn_{0.75}Ru_{0.25}$)O_2. (b) EDS mapping of CNT-($Mn_{0.75}Ru_{0.25}$)O_2. (c) High-magnification STEM image showing the morphology from (a). (d) Atomic-resolution STEM image of a representative part selected from (c). (e) Enlarged view of the red-boxed region in (d). (f-h) the corresponding intensity profile of the line regions in (e).

comparing ($Mn_{0.75}Ru_{0.25}$)O_2 with commercial RuO_2, the Ru $3p_{3/2}$ peak of ($Mn_{0.75}Ru_{0.25}$)O_2 undergoes a 0.4 eV negative shift, indicating that Ru is in a partially reduced state. The opposite shifts between Mn and Ru confirm the existence of electron coupling through the oxygen bridge, with electrons transferring from Mn to Ru. Additionally, the Ru $3p_{3/2}$ peak of CNT-($Mn_{0.75}Ru_{0.25}$)O_2 shows a 0.2 eV negative shift compared to ($Mn_{0.75}Ru_{0.25}$)O_2 (Figure 2b). Taken together, these shifts confirm that in CNT-($Mn_{0.75}Ru_{0.25}$)O_2, electrons transfer from C to Mn and then to Ru through the Mn-O bridge. In addition, the progressive increase in work function across CNT, MnO_2, (Mn_xRu_{1-x})O_2, and RuO_2 enables spontaneous electron transfer along this sequence, which is consistent with the observed XPS peak shifts and supports the proposed C to Mn to Ru charge redistribution.[26–28] This charge redistribution stabilizes Ru in a partially reduced state, which is expected to mitigate over-oxidation and dissolution under acidic OER conditions (Table S1 and S2)[29]. This effect also can effectively optimize the electronic structure of active sites, thereby modulating both activity and stability.[30–32]

The O K-edge soft X-ray absorption near-edge structure (XANES) spectra of CNT-($Mn_{0.75}Ru_{0.25}$)O_2 (Figure S4) exhibits a noticeable decrease in the intensity of the Ru-O hybridization peak and a negative energy shift relative to CNT-MnO_2, indicating an increased electron density localized on oxygen atoms. Meanwhile, the incorporation of Ru into CNT-MnO_2 increases the density of unoccupied states and lowers the t_2g/e_g ratio, which is known can enhance the adsorption of oxygenated intermediates. This electronic structure is consistent with the partial reduction of Ru species observed by XPS results[33,34].The Ru K-edge XANES spectra (Figure 2c) further support this conclusion. A distinct negative shift in the absorption edge of CNT-($Mn_{0.75}Ru_{0.25}$)O_2 relative to commercial RuO_2, indicating a lower Ru oxidation state. Moreover, the corresponding white line

View Article Online
DOI: 10.1039/D5SC04431F

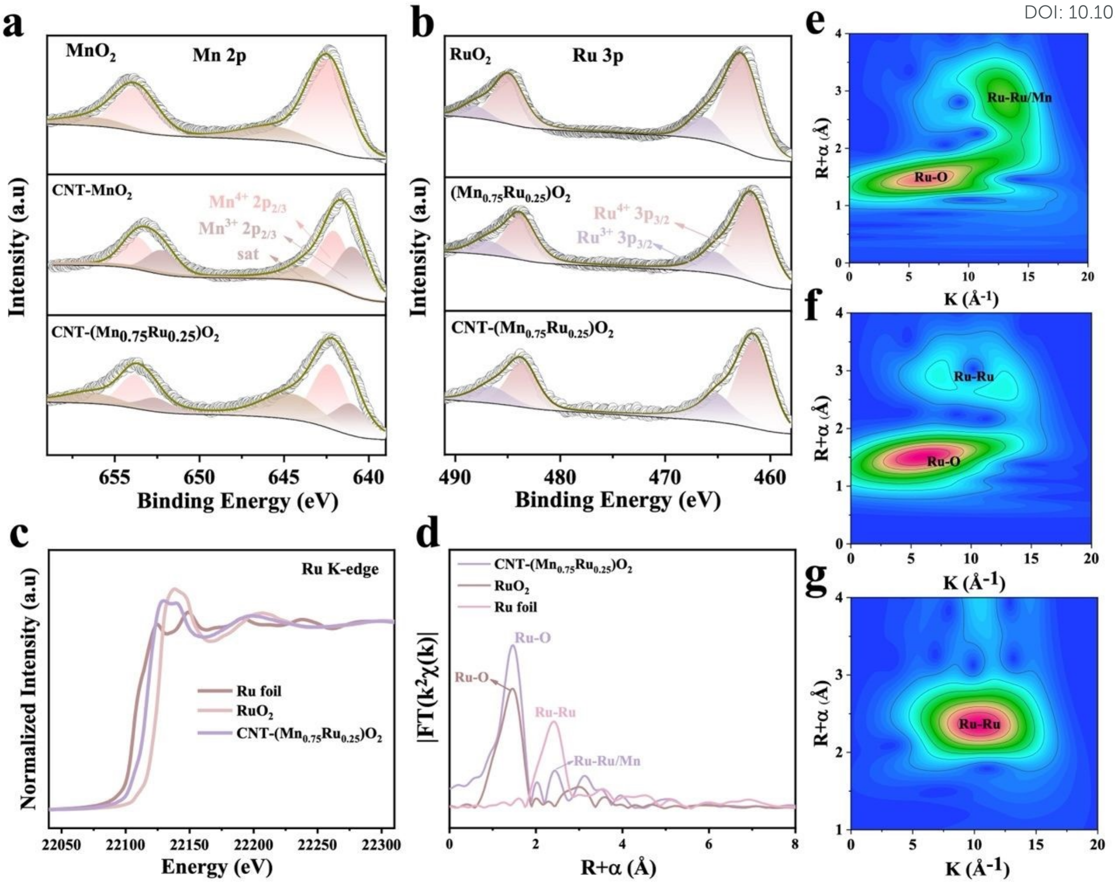

Figure 2. (a) Mn 2p XPS spectra of CNT-$(Mn_{0.75}Ru_{0.25})O_2$, CNT-MnO_2 and MnO_2. (b) Ru 3p XPS spectra of CNT-$(Mn_{0.75}Ru_{0.25})O_2$, $(Mn_{0.75}Ru_{0.25})O_2$ and RuO_2. (c) Ru K-edge XANES spectra of CNT-$(Mn_{0.75}Ru_{0.25})O_2$, RuO_2 and Ru foil. (d) The Fourier-transformed Ru K-edge EXAFS spectra of CNT-$(Mn_{0.75}Ru_{0.25})O_2$, RuO_2 and Ru foil. (e-g) The Wavelet transforms the Ru K-edge EXAFS signals of CNT-$(Mn_{0.75}Ru_{0.25})O_2$, RuO_2 and Ru foil.

intensity is also reduced, indicating a lower density of unoccupied Ru 4d states and weaker Ru-O hybridization. Fourier-transformed Ru K-edge EXAFS spectra (Figure 3d, Figures S5-S6 and Table S3) display coordination peaks at ~1.44 Å (Ru–O), ~2.42 Å (Ru–Ru/Mn), and ~2.39 Å (Ru–Ru). As revealed by Ru K-edge EXAFS fitting results, the Ru-O bond length in CNT-$(Mn_{0.75}Ru_{0.25})O_2$ (1.95 Å) is slightly shorter than that in RuO_2 (1.96 Å). This slight shortening can be rationalized by anisotropic Coulomb interactions induced by Mn incorporation into Ru local environment, which has been reported as a structural signature of solid-solution formation in Ru-Mn oxides.[53] Based on the comprehensive analysis above, the CNT-$(Mn_xRu_{1-x})O_2$ catalyst is consistent with a solid solution structure. And the corresponding coordination number of Ru-O bonds in CNT-$(Mn_{0.75}Ru_{0.25})O_2$ (2.9) is lower than that in RuO_2 (4.6) and Ru foil (4.6), indicating that the catalyst contains abundant oxygen vacancies. Wavelet transform (WT) analysis (Figures 2e–g) further validates the coexistence of Ru-O, Ru-Mn, and Ru-Ru coordination environments.[13] These XAS results and XPS analyses collectively confirm that the Ru sites in CNT-$(Mn_{0.75}Ru_{0.25})O_2$ are in an electron-rich state, which originates from CNT-to-Mn-to-Ru electron transfer and is stabilized by Mn-O bridges.

Electrocatalytic activity

The electrocatalytic performance of CNT-$(Mn_xRu_{1-x})O_2$ catalysts was systematically evaluated for the acidic oxygen evolution reaction (OER) in the O_2-saturated 0.1 M $HClO_4$ electrolyte, using a standard three-electrode configuration. Linear sweep voltammetry (LSV) measurements were conducted with carbon paper (1x1 cm^2) as the working electrode, a platinum wire as the counter electrode, and a reversible hydrogen electrode (RHE) as the reference electrode. All potentials were corrected for iR compensation to ensure accurate comparison. As shown in Figure 3a and Figure S7, CNT-$(Mn_{0.75}Ru_{0.25})O_2$ exhibits the lowest overpotential of 120 mV at 10 mA cm^{-2} and 270 mV at 400 mA cm^{-2}, significantly outperforming both the CNT-free $(Mn_{0.75}Ru_{0.25})O_2$ (200 mV at 10 mA cm^{-2}) and commercial RuO_2 benchmark (230 mV at 10 mA cm^{-2}). This enhancement demonstrates the critical role of the CNT support in dispersing the active sites and facilitating synergistic interactions between Mn and Ru. The inductively coupled plasma-optical emission spectrometry (ICP-OES) analysis confirms the low Ru content in the CNT-supported catalysts, with Ru loadings of 1.7 wt. %, 3.2 wt. %, 3.9 wt. %, and 4.9 wt. % for CNT-$(Mn_{0.9}Ru_{0.1})O_2$, CNT-$(Mn_{0.8}Ru_{0.2})O_2$, CNT-$(Mn_{0.75}Ru_{0.25})O_2$, and CNT-

View Article Online
DOI: 10.1039/D5SC04431F

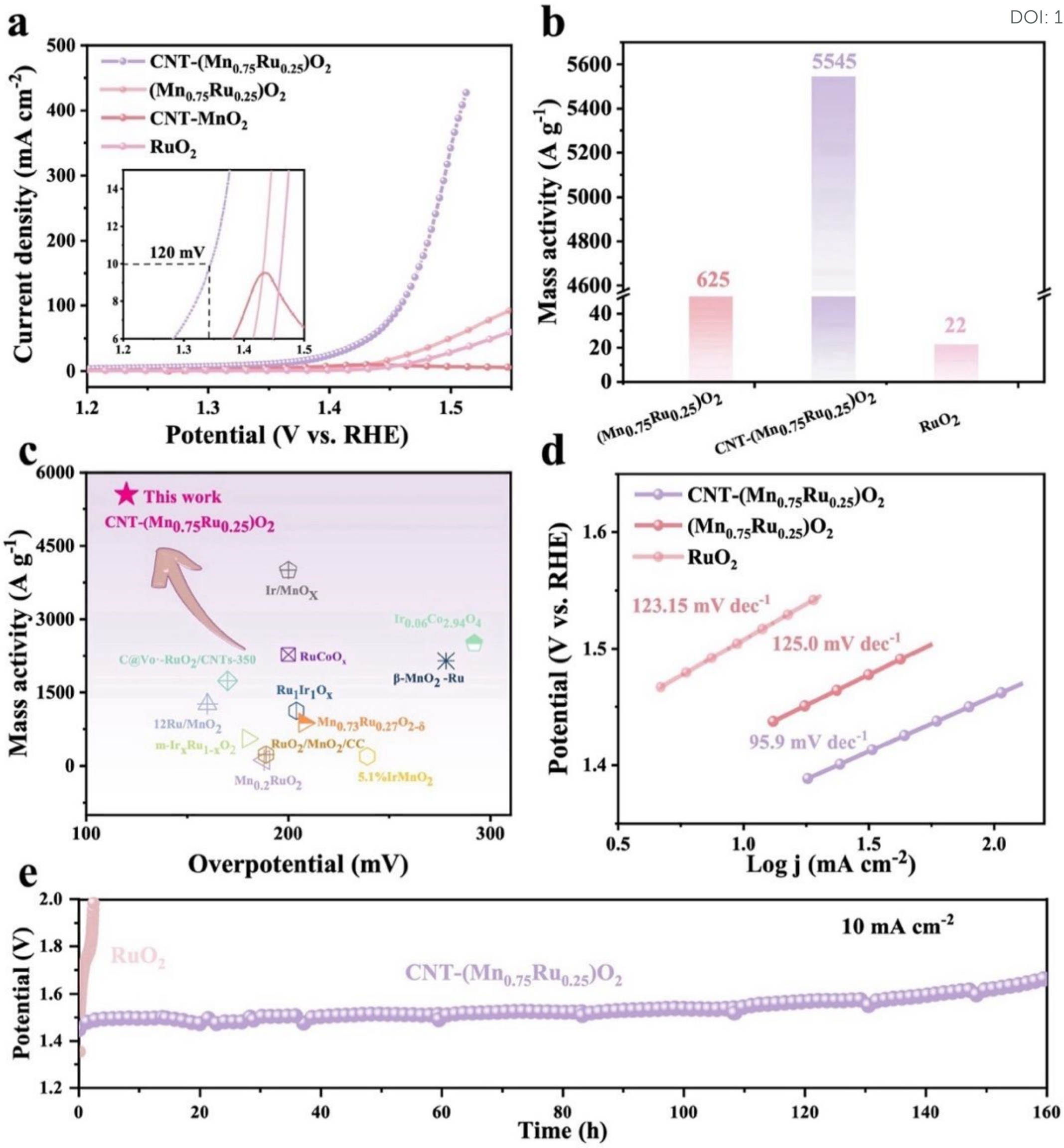

Figure 3. (a) OER performance of the catalysts in 0.1 M $HClO_4$ solution. (b) Mass activity at 1.5 V of the catalysts. (c) Comparison of OER overpotential and mass activity of previously reported electrocatalysts. (d) Tafel slop of the catalysts. (e) Durability test of CNT-$(Mn_{0.75}Ru_{0.25})O_2$ and RuO_2.

$(Mn_{0.7}Ru_{0.3})O_2$, respectively (Table S4). Notably, despite the low Ru content, CNT-$(Mn_{0.75}Ru_{0.25})O_2$ achieves a remarkable mass activity of 5549 A g_{Ru}^{-1} at 1.5 V vs. RHE, which is ~252 times higher than that of commercial RuO_2 (22 A g_{Ru}^{-1}) and substantially higher than most reported Ru-based catalysts (Figures 3b-c, Figure S8 and Table S5). Although the Ru content in CNT-$(Mn_{0.75}Ru_{0.25})O_2$ is 3.9 wt. %, the corresponding Ru loading on the carbon paper working electrode is only 0.077 mg cm^{-2}. At this low loading, the CNT-$(Mn_{0.75}Ru_{0.25})O_2$ delivers an overpotential of 120 mV at 10 mA cm^{-2}, along with outstanding mass activity (Table S6). This result highlights that the strategic incorporation of Ru into the MnO_2 matrix, mediated by the CNT support, enables efficient atomic dispersion of Ru and optimizes electronic interactions, thereby achieving exceptional catalytic performance at minimal noble metal content.

Kinetic analysis based on Tafel slopes further reveals that CNT-$(Mn_{0.75}Ru_{0.25})O_2$ exhibits the lowest slope of 95.9 mV dec^{-1}, significantly lower than those of commercial RuO_2 (123.1 mV dec^{-1}) and $(Mn_{0.75}Ru_{0.25})O_2$ (125.0 mV dec^{-1}, Figure 3d, Figure S9)[35]. This indicates that the CNT-Mn-Ru system effectively facilitates the reaction kinetics by modulating the electronic structure and lowering the energy barrier for the OER process. Electrochemical impedance spectroscopy (EIS) measurements (Figure S10) reveal that CNT-$(Mn_{0.75}Ru_{0.25})O_2$ possesses the lowest charge transfer resistance (R_{ct}) among all tested samples, further confirming the role of CNTs in providing a highly conductive network that accelerates electron transport.[36–38] The electrochemical surface area (ECSA), determined from the dependence of double-layer capacitance (C_{dl}) on different scan rates (5 mV s^{-1} to 25 mV s^{-1}), further supports the enhanced activity of CNT-$(Mn_{0.75}Ru_{0.25})O_2$. CNT-

View Article Online
DOI: 10.1039/D5SC04431F

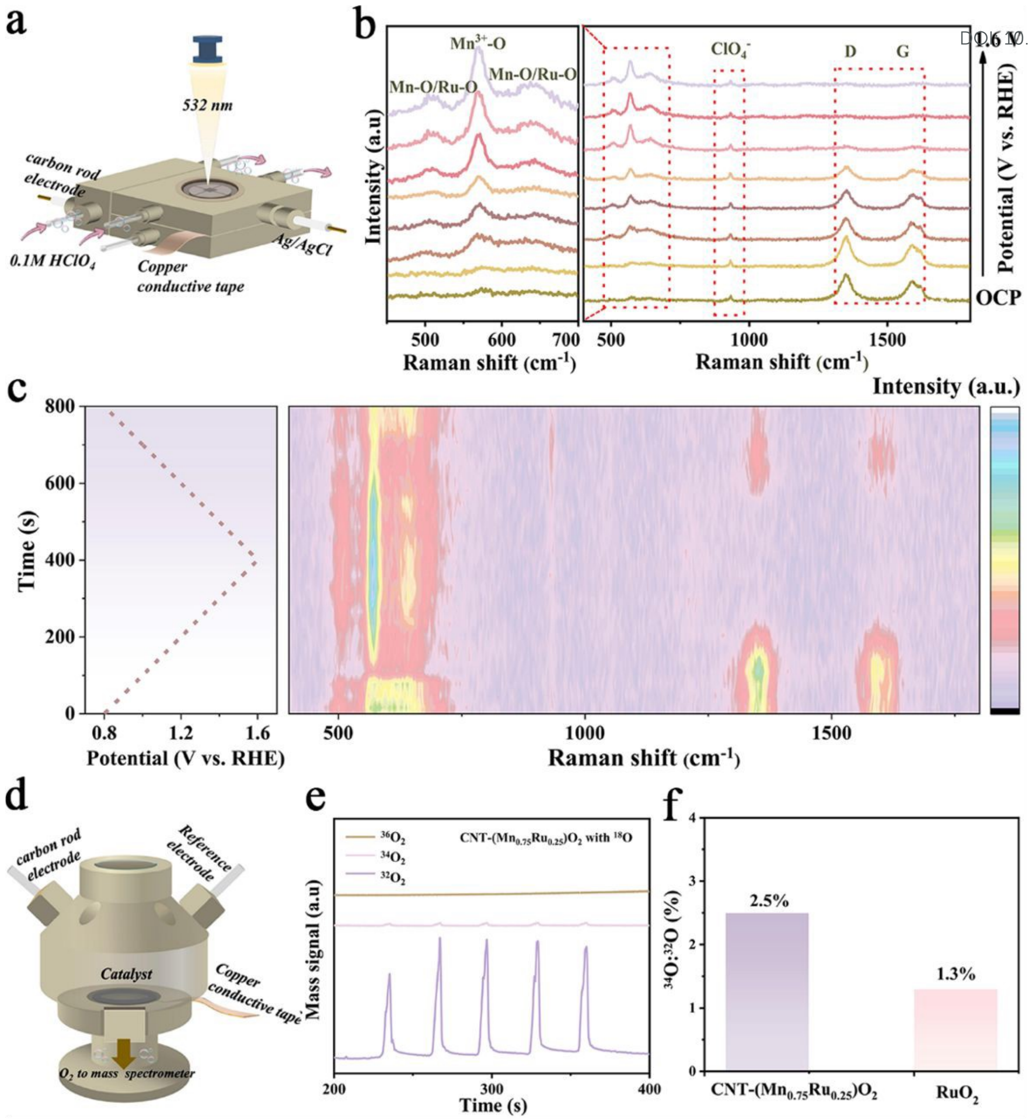

Figure 4. (a) Schematic of the in-situ Raman spectroscopy setup. (b) In-situ Raman spectra of CNT-$(Mn_{0.75}Ru0_{.25})O_2$ collected at increasing potentials from OCP to 1.6 V vs. RHE. (c) Corresponding Raman contour plots of CNT-$(Mn_{0.75}Ru_{0.25})O_2$ during CV cycling from 0.8V-1.6 V vs. RHE at 1 mV s^{-1}. (d) Schematic of the DEMS setup. (e) Mass spectrometry traces of $^{32}O_2$, $^{34}O_2$, and $^{36}O_2$ signals during potential cycling of CNT-$(Mn_{0.75}Ru_{0.25})O_2$ in $H_2{}^{16}O$-$HClO_4$ electrolyte. (f) Comparison of the $^{34}O_2/^{32}O_2$ peak area ratio of CNT-$(Mn_{0.75}Ru_{0.25})O_2$ and RuO_2.

$(Mn_{0.75}Ru_{0.25})O_2$ exhibits an ECSA of 159.9 mF cm^{-2}, which is 7.5 and 10.5 times higher than $(Mn_{0.75}Ru_{0.25})O_2$ (21.3 mF cm^{-2}) and commercial RuO_2 (15.2 mF cm^{-2}), respectively (Figures S11-S12).[34,39] This substantial increase reveals the dual role of CNT: promoting high-density dispersion of active sites and maximizing their electrochemical accessibility. Long-term durability tests under a constant current density (10 mA cm^{-2}, Figure 3e) demonstrate that CNT-$(Mn_{0.75}Ru_{0.25})O_2$ maintains stable operation for over 160 hours. To evaluate catalyst degradation, ICP-OES analysis of the post-electrolysis electrolyte revealed that only 4.9% of Ru was dissolved, substantially lower than the ~19% reported for commercial RuO_2 under similar acidic conditions, indicating enhanced resistance to Ru dissolution under acidic OER conditions.[40] In contrast, commercial RuO_2 suffers from rapid degradation, with significant activity loss observed within 3 hours. Meanwhile, CV tests at different scan rates were performed on the post-stability sample. The C_{dl} (Figure S13) decreased by approximately 26 % compared with the sample before stability test. Combined with ICP and HAADF-STEM analysis, the decrease in double-layer capacitance supports the conclusion that catalysts agglomeration occurred during the stability test To further understand the origin of performance decay after 160 h, TEM and HAADF-STEM images (Figure S14) show that the homogeneous $Mn_xRu_{1-x}O_2$ solid solution structure is maintained. The initially uniform distribution became more aggregated on the CNT surface, indicating particle growth. XRD analysis (Figure S15) reveals sharpened diffraction peaks, confirming increased crystallinity. This aggregation likely reduces the accessible active surface area, contributing to the observed decline in OER performance. Nonetheless, the well-dispersed $(Mn_xRu_{1-x})O_2$ architecture before operation plays a key role in achieving high activity at

View Article Online
DOI: 10.1039/D5SC04431F

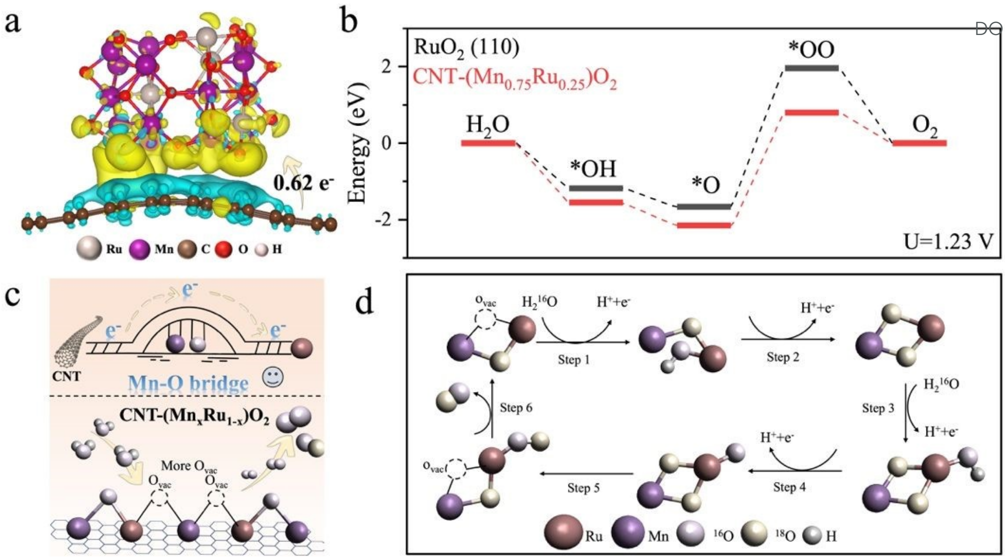

Figure5. (a) Charge distribution analysis of CNT-($Mn_{0.75}Ru_{0.25}$)O_2. Yellow regions indicates charge accumulation, while a blue regions indicates charge reduction.(b) The calculated reaction pathways of CNT-($Mn_{0.75}Ru_{0.25}$)O_2 and RuO_2(110) for acidic OER at U = 1.23 V. Schematic illustration of the LOM pathway during acidic OER (c-d) Enhanced LOM pathway in CNT-(MnxRu$_{1-x}$)O_2 with improved oxygen vacancy dynamics and structural stability.

low Ru content and future optimization will focus on mitigating particle growth to enhance durability.

Catalytic mechanism

To unravel the origin of the enhanced OER, we first examined the oxygen species in CNT-($Mn_{0.75}Ru_{0.25}$)O_2, ($Mn_{0.75}Ru_{0.25}$)O_2, CNT-MnO_2 and MnO_2 catalysts by XPS. As shown in Figure S16a, the O 1s spectra of all catalysts can be deconvoluted into three components corresponding to lattice oxygen (O_{lat}), oxygen vacancies (O_v), and adsorbed oxygen species (O_{ads}). Notably, the O_v percentage of CNT-($Mn_{0.75}Ru_{0.25}$)O_2 (60.4%) is significantly larger than that of other catalysts, indicating a higher concentration of oxygen vacancies in the CNT-Mn-Ru system. And the percentage of CNT-MnO_2 (28.8%) and ($Mn_{0.75}Ru_{0.25}$)O_2 (38.2%) are both larger than that of MnO_2 (18.8%), indicating CNT and Ru can promote the generation of more oxygen vacancies (Figure S16b). These results suggest that both the incorporation of Ru in MnO_2 and the CNT support facilitates the generation of oxygen vacancies. The observed increase in O_v concentration can be rationalized by the following mechanism. Oxygen vacancies in metal oxides can be introduced through cation doping or anion substitution. Incorporation of cations with lower oxidation states or lower oxygen vacancy formation energies tends to promote the formation of oxygen vacancies via a charge compensation mechanism. In this work, the introduction of low-valent Ru^{3+} into the MnO_2 lattice induces such a compensation process, thereby increasing the concentration of oxygen vacancies. [41] This defect engineering not only enhances the intrinsic activity by providing additional active sites for O-O coupling, but also modulates the surface electronic structure to favor intermediate adsorption during OER.[42,43]

The dynamic structural evolution of the catalyst under OER conditions was further investigated by *in-situ* Raman spectroscopy. Since the water band remains constant with increasing potential, all Raman spectra were normalized to the intensity of the water peak to minimize the effects of bubble interference and enable accurate comparison of intermediate-related features. As illustrated in Figure 4a, an H-type flow cell was used to monitor the real-time structural evolution of catalysts under potential control. The vibrational spectra of RuO_2 are observed in Figure S17, showing characteristic Ru-O stretching modes.[44] For the CNT-($Mn_{0.75}Ru_{0.25}$)O_2, the Raman peaks at 510cm^{-1} and 637 cm^{-1} are assigned to Mn-O/Ru-O stretching vibrations, while the peak at ~580 cm^{-1} corresponds to Mn^{3+}-O band, consistent with previous reports.[25,45–48] Additionally, carbon-related features are observed at ~1350 cm^{-1} (D band), ~1580 cm^{-1} (G band), and ~2700 cm^{-1} (2G band),[49,50] corresponding to defect-induced vibrations, in-plane sp^2 carbon stretching, and the second-order overtone, respectively. Notably, the intensities of Mn-O/Ru-O and Mn^{3+}-O vibrational modes increase markedly from 0.8 V to 1.6 V vs. RHE, reflecting the potential-dependent accumulation of lattice oxygen intermediates (Figure 4b). In addition, increasing peak intensity with the applied voltage suggest that the oxygen vacancies can participate in the progress of the reaction, whereas CNT-MnO_2 shows negligible spectral variation over the same potential range (Figures S18a). The corresponding contour plots (Figure 4c, Figure S18b) demonstrate reversible modulation of the characteristic peaks through CV cycling, indicating dynamic reconstruction of reversible oxygen vacancy changes of the CNT-($Mn_{0.75}Ru_{0.25}$)O_2 during OER, which is not occur in CNT-MnO_2. Notably, the CNT-($Mn_{0.75}Ru_{0.25}$)O_2 catalyst exhibits no significant red or blue shift of the Ru-O vibrational band under increasing potential, in contrast to the blue shift observed in CNT-MnO_2. This spectral invariance suggests that the formation of higher-valence Ru species is effectively inhibited, likely due to directional electron transfer mediated by Mn-O bridges. These bridges facilitate electron transfer from CNTs to Ru centers,

View Article Online
DOI: 10.1039/D5SC04431F

mitigating over-oxidation under acidic OER conditions and thereby enhancing catalyst durability.[52]These observations reveal that the Mn-O-Ru interaction plays a key role in enabling dynamic surface restricting under OER, which promotes the reversible binding of intermediates. Simultaneously, the CNT provides robust structural support, ensuring the stable dispersion of active sites throughout the reaction.[51]

To further probe the oxygen evolution pathway, we performed in situ differential electrochemical mass spectrometry (DEMS) measurements using ^{18}O-labeled catalysts CNT-$(Mn_{0.75}Ru_{0.25})O_2$ and commercial RuO_2 (Figure 4d). Prior to DEMS analysis, the catalysts were pre-labelled by CV cycling in 0.1 M $HClO_4$ prepared with $H_2{}^{18}O$. After the labelling process, the evolved O_2 during OER was monitored in a 0.1 M $HClO_4$ electrolyte prepared with $H_2{}^{16}O$, allowing us to distinguish lattice oxygen (^{18}O) and oxygen derived from water (^{16}O). The evolution of $^{36}O_2$ ($^{18}O^{18}O$), $^{34}O_2$ ($^{16}O^{18}O$) and $^{32}O_2$ ($^{16}O^{16}O$) was quantitatively tracked to probe the oxygen evolution mechanism of catalysts.[52,53] As shown in Figures 4e and S19, during the OER process of both catalysts, only $^{34}O_2$ and $^{32}O_2$ were detected, with no $^{36}O_2$ observed, confirming that both catalysts follow a lattice oxygen-mediated mechanism (LOM). The ratio of $^{34}O_2$ to $^{32}O_2$ (Figure 4f) for CNT-$(Mn_{0.75}Ru_{0.25})O_2$ was determined to be 2.5%, higher than that of commercial RuO_2 (1.3%), indicating greater lattice oxygen participation in the CNT-$(Mn_{0.75}Ru_{0.25})O_2$. This phenomenon is attributed to the abundant oxygen vacancies on the CNT-$(Mn_{0.75}Ru_{0.25})O_2$, which can be labelled by ^{18}O and then reversibly participate in the OER process. This trend aligns well with the higher oxygen vacancy concentration derived from XPS O 1s deconvolution and the potential-dependent reversibility observed in *in-situ* Raman spectroscopy, suggesting that the CNT-confined Mn-O-Ru framework stabilizes Ru sites in a partially reduced state and inhibits over-oxidation.[54,55]

To further explore the reaction mechanism, density functional theory (DFT) calculations were performed (Figures 5a-b and S20)[58]. Figure 5a presents the differential charge analysis results of CNT-$(Mn_{0.75}Ru_{0.25})O_2$ with Bader charge calculations showing that 0.62 e- transfer from CNT to $(Mn_{0.75}Ru0_{.25})O_2$. As shown in Figure 5b, the rate-determining step (RDS) for both CNT-$(Mn_{0.75}Ru_{0.25})O_2$ and RuO_2 involves the formation of *OO intermediate. The energy barrier for the RDS of CNT-$(Mn_{0.75}Ru_{0.25})O_2$ is lower than that of RuO_2 (110), indicating an improvement in the reaction kinetics. Combined with the experimental evidence from DFT calculations, it is shown that there exist a more favorable oxygen evolution pathways between CNT-$(Mn_{0.75}Ru_{0.25})O_2$ and commercial RuO_2. We believe that the classic LOM in RuO_2 involves direct participation of lattice oxygen in the O-O formation process. However, the highly symmetric rutile structure of RuO_2, while intrinsically active, renders it susceptible to excessive lattice oxygen activation under acidic OER conditions, promoting the formation of unstable RuO_4^{2-} intermediates (Figure S21).[56,57] This over-oxidation pathway inevitably accelerates Ru dissolution and compromises catalyst stability. In contrast, as shown in Figure 5c-d, the CNT-$(Mn_xRu_{1-x})O_2$ adopts a structurally and electronically distinct configuration that enables a more favorable LOM process.[58] The incorporation of Mn and the CNT support induces a highly dispersed architecture in which electron-rich Ru centers are stabilized by Mn-O bridges and abundant oxygen vacancies. These features synergistically enhance both activity and stability. On the one hand, the Mn-O bridges facilitate directional electron transfer from CNTs to Ru during OER, serving as a protective pathway that mitigates over-oxidation of the Ru under acidic conditions.[28] On the other hand, *in-situ* Raman spectroscopy corroborated that CNT-$(Mn_{0.75}Ru_{0.25})O_2$ exhibits reversible, potential-dependent modulation of the Mn-O/Ru-O and Mn^{3+}-O vibrational bands, while RuO_2 shows limited dynamic flexibility.[53] The enhanced and reversible Raman signals in CNT-$(Mn_xRu_{1-x})O_2$ suggest that oxygen vacancies not only provide additional adsorption sites for intermediates but also enable structural adaptability during OER cycling, facilitating efficient formation and desorption of *O species.[59–61]

Taken together, these results establish a coherent mechanistic framework: the synergistic combination of the CNT support, Mn incorporation, and Ru dispersion in CNT-$(Mn_xRu_{1-x})O_2$ creates a unique Mn-O-bridge network that enables directional electron transfer, modulates surface electronic states, and tunes oxygen vacancy concentration. This CNT-confined Mn-O-Ru framework effectively improve the usage of Ru atoms, mitigates Ru over-oxidation and dissolution, and promotes a more stable and efficient OER process under acidic conditions. In contrast, RuO_2 suffers from its symmetric crystal structure and strong lattice oxygen participation, which ultimately accelerates Ru leaching and deactivation.

Conclusions

In summary, we report a structurally engineered CNT-confined $(Mn_xRu_{1-x})O_2$ catalysts that achieves outstanding acidic OER performance at low Ru loading. The uniform nanoscale coating of $(Mn_xRu_{1-x})O_2$ along the CNT sidewalls not only promotes highly dispersed active sites and abundant oxygen vacancies, but also facilitates directional electron transfer through Mn-O bridges. This unique electronic architecture stabilizes Ru in a partially reduced state, effectively mitigating over-oxidation and dissolution pathways that typically plague Ru-based catalysts under acidic conditions. Combined spectroscopic and electrochemical analyses reveal that tuning the local electronic environment and oxygen vacancy concentration is essential for suppressing dissolution of Ru, thereby balancing catalytic activity and stability. This work highlights the importance of CNT confinement and Mn-O bridge-mediated electronic coupling in modulating Ru reactivity and durability. Overall, our findings establish a versatile design strategy for developing robust, high-performance acidic OER catalysts that decouple noble metal usage from activity, offering a promising pathway for advancing PEMWE technologies.

Author contributions

L. Z., H. L. and X. Z. conceived the research and wrote the paper. X. Z. and X. M. performed catalysts synthesis and general characterization. Z. Y. performed DEMS, supervised by Z. L. J. Y.

View Article Online
DOI: 10.1039/D5SC04431F

assisted X. Z. in the XAS measurements. L. Z. and H. L. supervised the research. All the authors contributed to the discussions and revisions of the manuscript.

Conflicts of interest

The authors declare no competing interests.

Data availability

The data that support the findings of this study are available on request from the corresponding author.

Acknowledgements

This work was financially supported by the National Natural Science Foundation of China (No. 22472101), Guangdong Science and Technology Department Program (2025A1515010455, 2021QN02L252), Research Team Cultivation Program of Shenzhen University (023QNT007) and Scientific Foundation for Youth Scholars of Shenzhen University (868-000001033351).

References

1 H. Su, C. Yang, M. Liu, X. Zhang, W. Zhou, Y. Zhang, K. Zheng, S. Lian and Q. Liu, *Nat. Commun.*, 2024, **15**, 95.

2 S. Kong, A. Li, J. Long, K. Adachi, D. Hashizume, Q. Jiang, K. Fushimi, H. Ooka, J. Xiao and R. Nakamura, *Nat. Catal.*, 2024, 1–10.

3 X. Ping, Y. Liu, L. Zheng, Y. Song, L. Guo, S. Chen and Z. Wei, *Nat. Commun.*, 2024, **15**, 2501.

4 A. Kumar, M. Gil-Sepulcre, J. Lee, V. Q. Bui, Y. Wang, O. Rüdiger, M. G. Kim, S. DeBeer and H. Tüysüz, *Adv. Mater.*, 2024, **36**, 2401648.

5 PGM prices and trading, https://matthey.com/products-and-markets/pgms-and-circularity/pgm-management, (accessed May 8, 2025).

6 J. Zhao, Y. Guo, Z. Zhang, X. Zhang, Q. Ji, H. Zhang, Z. Song, D. Liu, J. Zeng, C. Chuang, E. Zhang, Y. Wang, G. Hu, M. A. Mushtaq, W. Raza, X. Cai and F. Ciucci, *Nat. Nanotechnol.*, 2024, 57–66.

7 L. Chong, G. Gao, J. Wen, H. Li, H. Xu, Z. Green, J. D. Sugar, A. J. Kropf, W. Xu, X.-M. Lin, H. Xu, L.-W. Wang and D.-J. Liu, *Science*, 2023, **380**, 609–616.

8 L. Cao, Q. Luo, J. Chen, L. Wang, Y. Lin, H. Wang, X. Liu, X. Shen, W. Zhang, W. Liu, Z. Qi, Z. Jiang, J. Yang and T. Yao, *Nat. Commun.*, 2019, **10**, 4849.

9 K. Wang, Y. Wang, B. Yang, Z. Li, X. Qin, Q. Zhang, L. Lei, M. Qiu, G. Wu and Y. Hou, *Energy Environ. Sci.*, 2022, **15**, 2356–2365.

10 S. Zuo, Z.-P. Wu, D. Xu, R. Ahmad, L. Zheng, J. Zhang, L. Zhao, W. Huang, H. Al Qahtani, Y. Han, L. Cavallo and H. Zhang, *Nat. Commun.*, 2024, **15**, 9514.

11 Y. Xu, Z. Mao, J. Zhang, J. Ji, Y. Zou, M. Dong, B. Fu, M. Hu, K. Zhang, Z. Chen, S. Chen, H. Yin, P. Liu and H. Zhao, *Angew. Chem.Int. Ed.,* 2024, **136**, e202316029.

12 W. Hu, B. Huang, M. Sun, J. Du, Y. Hai, W. Yin, X. Wang, W. Gao, C. Zhao, Y. Yue, Z. Li and C. Li, *Adv. Mater.*, 2025, **37**, 2411709.

13 C. Zhou, L. Li, Z. Dong, F. Lv, H. Guo, K. Wang, M. Li, Z. Qian, N. Ye, Z. Lin, M. Luo and S. Guo, *Nat. Commun.*, 2024, **15**, 9774.

14 H. Yan, Z. Jiang, B. Deng, Y. Wang and Z.-J. Jiang, *Adv. Energy Mater.*, 2023, **13**, 2300152.

15 J. Yang, K. An, Z. Yu, L. Qiao, Y. Cao, Y. Zhuang, C. Liu, L. Li, L. Peng and H. Pan, *ACS Catal.*, 2024, **14**, 17739–17747.

16 J. Chang, Y. Shi, H. Wu, J. Yu, W. Jing, S. Wang, G. I. N. Waterhouse, Z. Tang and S. Lu, *J. Am. Chem. Soc.*, 2024, **146**, 12958–12968.

17 Q. Ma and S. Mu, *Interdiscip. Mater.*, 2023, **2**, 53–90.

18 C. Li, D. Li, L. Li, H. Yang, Y. Zhang, J. Su, L. Wang and B. Liu, *Adv. Mater.*, 2025, 2500416.

19 Y. N. Regmi, E. Tzanetopoulos, G. Zeng, X. Peng, D. I. Kushner, T. A. Kistler, L. A. King and N. Danilovic, *ACS Catal.*, 2020, **10**, 13125–13135.

20 J.-W. Zhao, K. Yue, H. Zhang, S.-Y. Wei, J. Zhu, D. Wang, J. Chen, V. Y. Fominski and G.-R. Li, *Nat. Commun.*, 2024, **15**, 2928.

21 C. Lin, J.-L. Li, X. Li, S. Yang, W. Luo, Y. Zhang, S.-H. Kim, D.-H. Kim, S. S. Shinde, Y.-F. Li, Z.-P. Liu, Z. Jiang and J.-H. Lee, *Nat. Catal.*, 2021, **4**, 1012–1023.

22 J. Kuang, B. Deng, Z. Jiang, Y. Wang and Z.-J. Jiang, *Adv. Mater.*, 2024, 2306934.

23 Z. Tao, N. Lv, H. Zhao, X. Luo, Z. Li, J. Yu, L. Chen, X. Liu and S. Mu, *Chem. Sci.*, 2024, **15**, 16796–16803.

24 J. Zhang, X. Cao, Y.-F. Jiang, S.-F. Hung, W. Liu, H. B. Yang, C.-Q. Xu, D.-S. Li, T. Zhang, Y. Li, J. Li and B. Liu, *Chem. Sci.*, 2022, **13**, 12114–12121.

25 Y. Qin, Y. Liu, Y. Zhang, Y. Gu, Y. Lian, Y. Su, J. Hu, X. Zhao, Y. Peng, K. Feng, J. Zhong, M. H. Rummeli and Z. Deng, *ACS Catal.*, 2023, **13**, 256–266.

26 V. Barone, J. E. Peralta, J. Uddin and G. E. Scuseria, *J. Chem. Phys.*, 2006, **124**, 024709.

27 H. Ago, T. Kugler, F. Cacialli, W. R. Salaneck, M. S. P. Shaffer, A. H. Windle and R. H. Friend, *J. Phys. Chem. B*, 1999, **103**, 8116–8121.

28 X. Wu, C. Lin, W. Hu, C. Fu, L. Tan, H. Wang, F. Meharban, X. Pan, P. Fu, H.-D. Um, Q. Xiao, X. Li, M. Yamauchi and W. Luo, *Small Struct.*, 2024, **5**, 2300518.

29 E. Naranjo, B. Abd Alreda, M. Zaidi, K. M. Batoo, S. Hussain, A. A. Almulla, A. A. Al-Sattar Dawood, S. G. Al- Musawi, M. F. Ramadan, S. A. Hamood, S. H. Zain Al-Abdeen, R. S. Zabibah and A. Alsalamy, *J. Phys. Chem. Solids*, 2024, **187**, 111856.

30 W. Wu, Y. Wang, S. Song, Z. Ge, C. Zhang, J. Huang, G. Xu, N. Wang, Y. Lu, Z. Deng, H. Duan, M. Liu and C. Tang, *Angew. Chem. Int. Ed.*, 2025, **64**, e202504972.

31 K. Wang, C. Ni, L. Jin, X. Qian, H. Xu, H. Chen and G. He, *Chem. Sci.*, 2025, **16**, 7467–7476.

32 C. Zhu, Y. Wang, Z. Jiang, F. Xu, Q. Xian, C. Sun, Q. Tong, W. Zou, X. Duan and S. Wang, *Appl. Catal. B Environ.*, 2019, **259**, 118072.

33 H. Wu, Z. Fu, J. Chang, Z. Hu, J. Li, S. Wang, J. Yu, X. Yong, G. I. N. Waterhouse, Z. Tang, J. Chang and S. Lu, *Nat. Commun.*, 2025, **16,** 4482.

34 G. Chen, R. Lu, C. Ma, X. Zhang, Z. Wang, Y. Xiong and Y. Han, *Angew. Chem. Int. Ed.*, 2024, **63**, e202411603.

35 S. Anantharaj, S. Noda, M. Driess and P. W. Menezes, *ACS Energy Lett.*, 2021, **6**, 1607–1611.

36 B. Zhang, J. Wang, G. Liu, C. M. Weiss, D. Liu, Y. Chen, L. Xia, P. Zhou, M. Gao, Y. Liu, J. Chen, Y. Yan, M. Shao, H. Pan and W. Sun, *Nat. Catal.*, 2024, **7**, 441–451.

37 A. Ch. Lazanas and M. I. Prodromidis, *ACS Meas. Sci. Au*, 2023, **3**, 162–193.

38 J. Huang, Y. Gao, J. Luo, S. Wang, C. Li, S. Chen and J. Zhang, *J. Electrochem. Soc.*, 2020, **167**, 166503.

39 W. Zhao, F. Xu, L. Liu, M. Liu and B. Weng, *Adv. Mater.*, 2023, 2308060.

40 Y. Qin, T. Yu, S. Deng, X.-Y. Zhou, D. Lin, Q. Zhang, Z. Jin, D. Zhang, Y.-B. He, H.-J. Qiu, L. He, F. Kang, K. Li and T.-Y. Zhang, *Nat. Commun.*, 2022, **13**, 3784.

View Article Online
DOI: 10.1039/D5SC04431F

41 G. Zhuang, Y. Chen, Z. Zhuang, Y. Yu and J. Yu, *Sci. China Mater.*, 2020, **63**, 2089–2118.

42 H. Li, X. Hu, L. Wang, L. Shi, T. T. Isimjan and X. Yang, *Chem. Eng. J.*, 2024, **481**, 148547.

43 X. Huang, C. Lee, Y. Li, J. Xu and D. Liu, *ACS Appl. Nano Mater.*, 2024, **7**, 9244–9251.

44 L. Wu, Q. Liang, J. Zhao, J. Zhu, H. Jia, W. Zhang, P. Cai and W. Luo, *Chin. J. Catal.*, 2023, **55**, 182–190.

45 D. Wang, F. Lin, H. Luo, J. Zhou, W. Zhang, L. Li, Y. Wei, Q. Zhang, L. Gu, Y. Wang, M. Luo, F. Lv and S. Guo, *Nat. Commun.*, 2025, **16**, 181.

46 Z. Lei, F. Shi and L. Lu, *ACS Appl. Mater. Interfaces*, 2012, **4**, 1058–1064.

47 S. Pan, H. Li, D. Liu, R. Huang, X. Pan, D. Ren, J. Li, M. Shakouri, Q. Zhang, M. Wang, C. Wei, L. Mai, B. Zhang, Y. Zhao, Z. Wang, M. Graetzel and X. Zhang, *Nat. Commun.*, 2022, **13**, 2294.

48 J. Liu, T. Wang, M. Sun, M. Liao, S. Wang, S. Liu, H. Shi, Y. Liu, Y. Shen, R. Cao, Y. Huang, B. Huang and Q. Li, *J. Am. Chem. Soc.*, 2024, **146**, 33276–33287.

49 S. Kaushal, A. K. Sahu, M. Rani and S. R. Dhakate, *Renew. Energy*, 2019, **142**, 604–611.

50 X. Feng, J. Liu, L. Chen, Y. Kong, Z. Zhang, Z. Zhang, D. Wang, W. Liu, S. Li, L. Tong and J. Zhang, *J. Am. Chem. Soc.*, 2023, **145**, 10259–10267.

51 M. Qi, X. Du, X. Shi, S. Wang, B. Lu, J. Chen, S. Mao, H. Zhang and Y. Wang, *J. Am. Chem. Soc,.*2025 **147** (21), 18295-18306

52 X. Chen, X.-T. Wang, J.-B. Le, S.-M. Li, X. Wang, Y.-J. Zhang, P. Radjenovic, Y. Zhao, Y.-H. Wang, X.-M. Lin, J.-C. Dong and J.-F. Li, *Nat. Commun.*, 2023, **14**, 5289.

53 Z. Li, H. Sheng, Y. Lin, H. Hu, H. Sun, Y. Dong, X. Chen, L. Wei, Z. Tian, Q. Chen, J. Su and L. Chen, *Adv. Funct. Mater.*, 2024, 2409714.

54 W. He, X. Tan, Y. Guo, Y. Xiao, H. Cui and C. Wang, *Angew. Chem. Int. Ed.*, 2024, **63**, e202405798.

55 L. Wu, W. Huang, D. Li, B. Zhao, H. Zhou and W. Luo, *Angew. Chem. Int. Ed.*, 2025, e202420848.

56 J. Fan, X. Zhang, M. Han, X. Xiang, C. Guo, Y. Lin, N. Shi, D. Xu, Y. Lai and J. Bao, *Small*, 2024, **20**, 2303927.

57 Z.-X. Qian, G.-H. Liang, L.-F. Shen, G. Zhang, S. Zheng, J.-H. Tian, J.-F. Li and H. Zhang, *J. Am. Chem. Soc.*, 2025, **147**, 1334–1343.

58 H. Liu, Q. Zhou, J. Yu, M. Nakabayashi, Y.-T. Lee, N. Shibata, Y. Li and J.-J. Delaunay, *ACS Catal.*, 2025, **15**, 8511–8521.

59 Y. Wang, X. Lei, B. Zhang, B. Bai, P. Das, T. Azam, J. Xiao and Z.-S. Wu, *Angew. Chem. Int. Ed.*, 2024, **63**, e202316903.

60 Y. Qin, X. Niu, R. Zhao, J. Sun, Z. Xu, Z. Guo, D. Liu, L. Guo, C. Liu, J. Zhang and Q. Wang, ACS Catal.,2024, **14**, 12970-12981.

61 T. Zhang, H.-F. Zhao, Z.-J. Chen, Q. Yang, N. Gao, L. Li, N. Luo, J. Zheng, S.-D. Bao, J. Peng, X. Peng, X.-W. Liu and H.-B. Yu, *Nat. Commun.*, 2025, **16**, 3327.

62 L. An, C. Wei, M. Lu, H. Liu, Y. Chen, G. G. Scherer, A. C. Fisher, P. Xi, Z. J. Xu and C.-H. Yan, *Adv. Mater.,* 2021, **33**, 2006328.

63 F.-Y. Chen, Z.-Y. Wu, Z. Adler and H. Wang, Joule, 2021, **5**, 1704–1731.

View Article Online
DOI: 10.1039/D5SC04431F

The datasets are available from the corresponding author on reasonable request.